

# Multiparameter two-dimensional inversion of scattered teleseismic body waves

## 2. Numerical examples

J. Shragge,<sup>1</sup> M. G. Bostock, and S. Rondenay<sup>2</sup>

Department of Earth and Ocean Sciences, University of British Columbia, Vancouver, British Columbia, Canada

**Abstract.** In this paper, we investigate the formal inversion of synthetic teleseismic  $P$  coda waves for subsurface elastic properties using a ray theoretic approach which assumes single scattering [Bostock *et al.*, this issue]. We consider a model comprising an idealized lithospheric suture zone whose geometrical configuration is drawn from previous deep crustal seismic studies. Two-dimensional, pseudospectral synthetic seismograms representing plane waves propagating through this model are preprocessed to extract an estimate of the scattered wave field generated by short-wavelength structure. These data are employed in a series of numerical simulations which examine the dependence of multiparameter inversion results on a range of input parameters. In particular, we demonstrate (1) the contrasting sensitivity which forward and backscattered waves display to structural recovery, (2) the diminution of the problem null-space accompanied by increased source coverage, (3) improvements in model reconstruction achieved through simultaneous treatment of multiple scattering modes, and (4) the robustness of the method for data sets with noise levels and receiver geometries that approach those of field experiments.

### 1. Introduction

Advances in our understanding of the continental lithosphere and underlying upper mantle have relied heavily on studies involving multichannel processing of teleseismic body wave data, most notably  $P$  wave travel time tomography [e.g., VanDecar, 1991]. Recent investigations [e.g., Revenaugh, 1995; Bostock, 1998; Ryberg and Weber, 2000], however, indicate that further insight into detailed lithospheric structure is to be obtained through multichannel analysis of secondary forward scattered waves in the  $P$  coda. Moreover, free-surface reflected and converted waves can also be considered as additional (and complementary) sources that may be exploited to constrain subsurface structure. Motivated by these postulates, a close analogy with industry-oriented methodology [e.g., Beylkin and Burridge, 1990], and the increasing availability of portable, three-component broadband sensors, a framework has been developed for the formal inversion/migration of teleseismic body waves for elastic parameters [Bostock *et al.*, this issue] (hereinafter referred to as paper 1) which assumes high-frequency, single scattering and is designed for practical implementation [see Rondenay *et al.*, this issue] (hereinafter referred to as paper 3).

To fully exploit the higher frequencies present in the  $P$  coda and to avoid spatial aliasing requires a dense spatial sampling ( $\sim 5$  km or less). The numbers of broadband sensors that can be readily accessed at the present time essentially precludes the possibility of fully three-dimensional (3-D), anisotropic, elastic inversion. In paper 1, we have, accordingly, rendered the problem practically tractable through the assumption of 2-D,

isotropic, elastic structure. The flexibility and utility of our approach are, moreover, enhanced through (1) provision for incident waves from arbitrary back azimuths, (2) allowance for independent appraisal of contributions from individual scattering mode interactions including the backscattered response afforded by the free surface, and (3) a tolerance for irregular source and receiver sampling including simultaneous treatment of multiple events.

Our objective in this paper is to investigate the potential of this inversion methodology through a series of numerical simulations. Specifically, our desire is to evaluate the performance of the algorithm in a controlled, idealized environment and to provide insight into limitations and potential problems that may arise during inversion of field data (i.e., paper 3). To this end, we have designed a number of synthetic 2-D simulations comprising interaction of upward propagating plane waves with a model lithospheric suture zone. This class of structure is a typical target in lithospheric-scale geophysical surveys [e.g., Cook *et al.*, 1998] and one which produces a response sufficiently complex that conventional teleseismic processing (i.e., receiver function) approaches may yield results which are not straightforward to interpret. Suture zones are, moreover, dominantly 2-D in geometry, and a 2-D inversion approach is therefore appropriate. For computational convenience we restrict consideration to in-plane propagation. Inclusion of obliquity (as permitted by our approach) would not affect the main conclusions of this paper, though it is, of course, essential in the treatment of field data as it permits the analysis of a full suite of global seismicity.

We begin our study with a brief summary of our idealized collisional suture model and proceed to describe the forward modeling of teleseismic  $P$  wave propagation through the model using a pseudospectral approach [Kosloff *et al.*, 1990]. This is followed by an outline of the preprocessing required to prepare the raw displacement seismograms for inversion. Various simplifications to the equations of paper 1 that arise from the in-plane geometry are then discussed. The results of a series of numerical simulations are subsequently presented with the objective of

<sup>1</sup>Now at Hager GeoScience Inc., Woburn, Massachusetts, USA.

<sup>2</sup>Now at Department of Geological Sciences, Brown University, Providence, Rhode Island, USA.

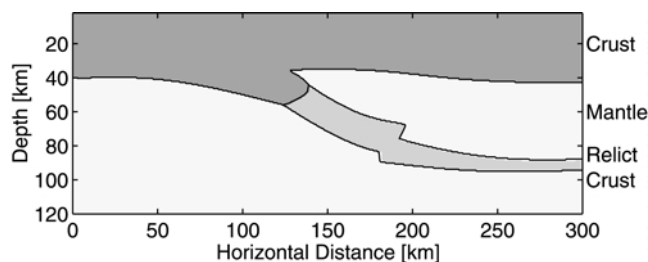


**Figure 1.** Idealized, three-component, collisional suture model. Velocities and densities of each material are given in Table 1.

identifying the importance of the roles that various parameters play in the recovery of structure. The paper concludes with a summary of key results.

## 2. Lithospheric Suture Model

Lithospheric suture zones are the signatures of collisions between continents which generally culminate extended periods of ocean-continent subduction. As such, they represent one of the more complex structures likely to be encountered in studies of the continental lithosphere. Although seismic reflection profiles have generally provided the most detailed views of lithospheric sutures [e.g., *Cook et al.*, 1998], they are limited in at least two respects. First, the use of anthropogenic sources limits depth penetration to uppermost mantle levels. Second, the narrow and relatively high signal bandwidth of conventional seismic sources often precludes accurate determination of signal polarity and hence the sign of impedance contrasts. Densely sampled teleseismic profiles would not suffer from these limitations to the same degree and, accordingly, could provide important complementary information on collisional sutures and other complex lithospheric structures.

Our idealized lithospheric suture model, shown in Figure 1, is defined over a  $300 \times 120$  km<sup>2</sup> section and consists of three materials with differing elastic properties. A low-velocity crustal layer overlies a faster upper mantle (see Table 1 for model velocities and densities). At the location of the suture, crustal material from the lithospheric block to the left bifurcates, with the lower segment descending into the mantle. At a depth of  $\sim 40$  km, it converts to velocities and density higher than the surrounding mantle (note the proportionally greater increase in  $S$  velocity) and thereafter folds and thins to the right of the model. Heterogeneity comprises both dipping, locally planar interfaces (i.e., the slowly varying Moho, subducting segments), from which specular conversions and reflections are expected, and sharper, angular discontinuities (i.e., mantle wedge, slab fold), which will produce more complex scattering, loosely referred to here as diffraction. Thus the model should afford a reasonable test of the algorithm's ability to image a range of structural heterogeneity.

## 3. Synthetic Seismograms

Several sets of two-component seismograms were computed through the lithospheric model described above using a 2-D, elastic pseudospectral code [*Kosloff et al.*, 1990]. The model was discretized at 0.6-km intervals in both directions which, given the minimum velocity in our model ( $3.6$  km s<sup>-1</sup>), allows for frequencies up to 4.0 Hz to be accurately modeled. This value corresponds approximately to the upper frequency limit of  $P$  wave seismograms from teleseismic events.

The seismograms comprise a suite of plane  $P$  waves interacting with the suture model at a range of incident horizontal slownesses,  $p_1^0 = [0.05, -0.05, 0.06, -0.06, 0.07, -0.07]$  s km<sup>-1</sup>. A

Gaussian waveform,  $e^{-18t^2}$  ( $t$  measured in seconds), was chosen to approximate the incident delta function pulse (i.e., Green's function) required in the inverse formulation. The planar wave front is a close approximation to that of a teleseismic  $P$  wave front predicted from spherical Earth models where the change in horizontal slowness over a 300-km interval at the Earth's surface will not generally exceed a few percent. The output seismogram sections consist of 600 traces recorded at the free surface. These sections are subsequently desampled by a factor of 5 to yield data sections of 120 traces, sampled at 3-km intervals, as input for inversion. To allow incorporation of the free-surface backscattered response, the duration spanned by individual records is  $\sim 50$  s after the direct arrival.

## 4. Preprocessing and Synthetic Results

Implementation of the method in paper 1 requires that we are able to effectively isolate the so-called scattered wave field  $\Delta \mathbf{u}$  (see equations (24), (25), and (43)–(45) of paper 1). The approach adopted here is that of *Bostock and Rondenay* [1999], who detail a procedure through which the incident wave field  $\mathbf{u}^0$  (i.e., the  $P$  wave field which would propagate in a smoothly varying 1-D reference medium) is approximately removed from a multichannel seismogram section to yield an estimate of the scattered wave field. The method may be summarized as follows: (1) the raw data sections,  $\mathbf{u} = [u_1, u_2]$ , are transformed into upgoing  $P$  and  $S$  wave field sections,  $\mathbf{w} = [P, SV]$ , via the free-surface transfer matrix [*Kennett*, 1991], (2) multichannel cross correlation [*VanDecar and Crosson*, 1990] is applied to a window about the direct (high-pass-filtered)  $P$  arrival to allow optimal alignment of the wave field sections, (3) the aligned  $P$  section is decomposed into its principal components through diagonalization of the zero-lag, cross-correlation matrix, (4) the first (or first few) principal component(s) are identified with the source time function of the incident wave field, while the remaining principal components (or some selection thereof) are associated with the scattered wave field, (5) the scattered displacement sections are reconstituted from the  $P$  and  $S$  wave field sections using the inverse free-surface transfer matrix, and (6) in practice, individual source time function estimates are then deconvolved from the scattered displacement to yield the scattered wave field  $\Delta \mathbf{u}$ ; however, we forego this step here as our Gaussian source-time function is essentially a low-pass-filtered approximation of the delta function required by theory. This approach obviates the problem of incomplete separation of incident and scattered  $P$  wave fields which is encountered in the treatment of field data (see discussion by *Bostock and Rondenay* [1999]) and allows us to concentrate on issues related to inversion rather than preprocessing. An analysis of incomplete wave field separation on real data is provided in paper 3. The final stage of preprocessing entails a convolution of  $\Delta \mathbf{u}$  with a filter whose frequency domain representation is  $F(\omega) = -i \text{sgn}(\omega) / \sqrt{-i\omega}$  (dictated by the geometrical configuration, plane wave source and 2-D heterogeneity) to produce a new time series  $\mathbf{v}$  (equation (29) in paper 1) to directly image jumps in elastic properties across discontinuities. Each trace is then subjected to a band-pass Butterworth filter between 0.1 and 4.0 Hz to approximate the typical frequency bandwidth from a deep teleseismic event.

**Table 1.** Lithospheric Model Parameters

Parameter	$P$ Wave Velocity, km s <sup>-1</sup>	$S$ Wave Velocity, km s <sup>-1</sup>	Density, g cm <sup>-3</sup>
Crust	6.2	3.6	2.8
Mantle	8.0	4.5	3.2
Relict crust	8.1	4.9	3.3

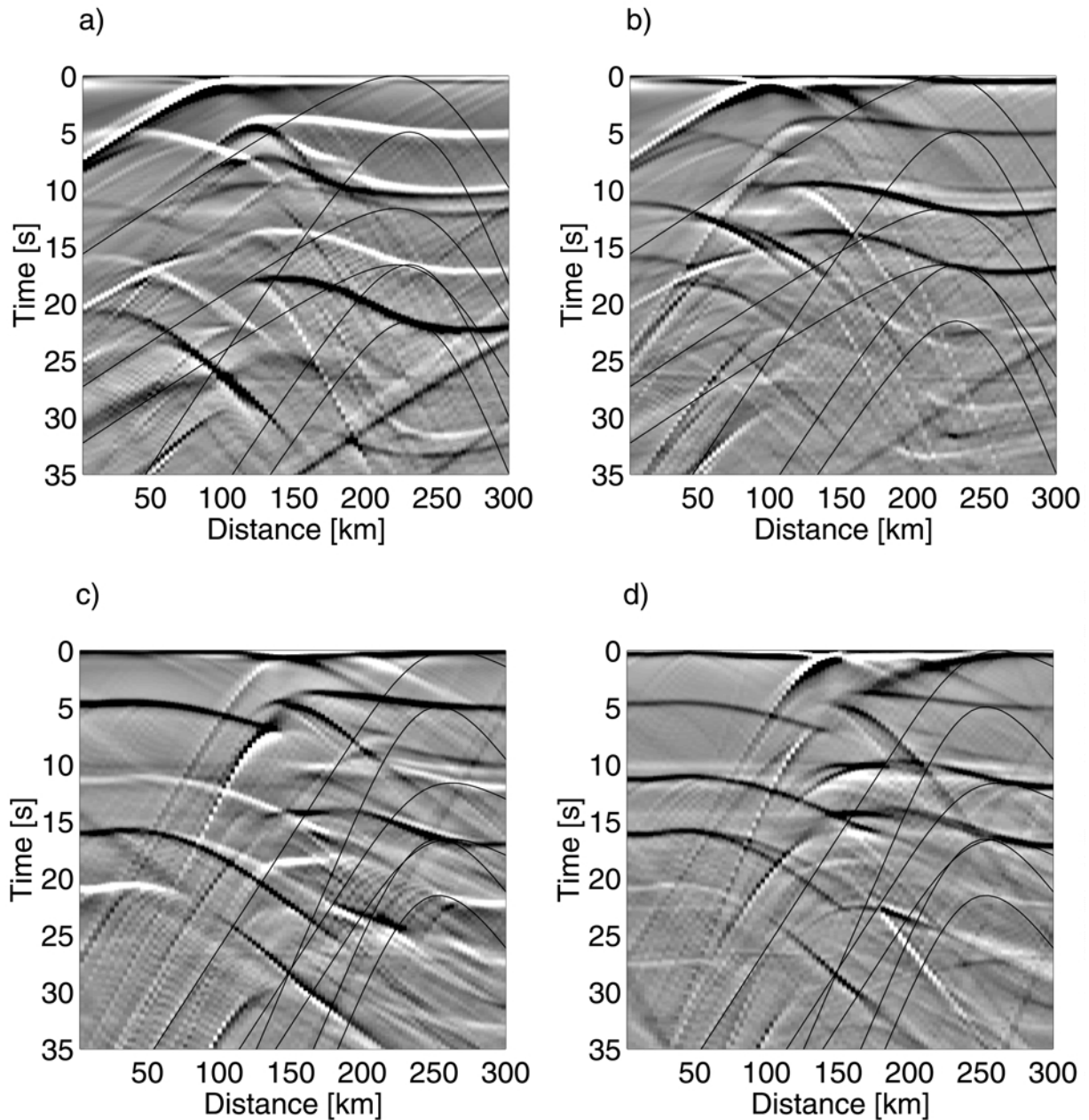


**Figure 2.** Preprocessed (but prior to filtering by  $F(\omega)$ ) synthetic seismogram sections generated for the idealized suture model in Figure 1. (a)  $\Delta u_1$  and (b)  $\Delta u_3$  components for an incident plane wave with horizontal slowness  $p_1^0 = -0.07 \text{ s km}^{-1}$ ; (c)  $\Delta u_1$  and (d)  $\Delta u_3$  components for an incident plane wave with horizontal slowness  $p_1^0 = 0.07 \text{ s km}^{-1}$ . Examples of travel time curves,  $T^q$  ( $q = 1, 2, 3, 4, 5, 6$  in order of increasing time) are superposed for model point  $\mathbf{x} = (240 \text{ km}, 40 \text{ km})$ .

Two-component, processed (but prior to application of  $F(\omega)$ ) scattered displacement waveforms (i.e.,  $\Delta \mathbf{u}$ ) for incident horizontal slownesses,  $p_1^0$ , of  $-0.07$  and  $0.07 \text{ s km}^{-1}$  are shown in Figures 2a–2d. Individual scattered phases apparent in Figures 2a–2d include both forward scattered waves ( $q = 1, 2$ ; equations (24) and (25) of paper 1), and backscattered waves ( $q = 3, 4, 5, 6, 7$ ; equations (24), (25), and (43)–(45) of paper 1) afforded through free-surface reflection of the incident upgoing  $P$  wave field into downgoing  $P$  and  $S$  waves. To summarize (see also Table 1 of paper 1),  $q = 1, 3$  represent  $P$ - $P$  scattering;  $q = 2, 4$  represent  $P$ - $S$  scattering;  $q = 5$  represents  $S$ - $P$  scattering; and  $q = 6, 7$  represent different modes of

$S$ - $S$  scattering (only one  $S$ - $S$  scattering mode,  $q = 6$ , is required for the in-plane, 2-D geometry of the present problem). The horizontal component response for right incidence (Figure 2a) is dominated by a  $P$ - $S$  conversion ( $q = 2$ ) from the Moho arriving at  $\sim 5$  s and a  $P$ - $P$  diffraction ( $q = 1$ ) centered at 100 km with apex at  $\sim 0$  s. Subsequent arrivals are most obvious on seismograms to the right of the suture: (1) a combination of  $P$ - $S$  ( $q = 2$ ) scattering originating from either side of the subducted crustal segment at  $\sim 10$ – $11$  s; (2) a backscattered  $P$ - $S$  conversion ( $q = 4$ ) from the Moho at  $\sim 17$  s; and (3) a  $S$ - $S$  reflection ( $q = 6$ ) from the Moho at  $\sim 22$  s. The vertical

component (Figure 2b) emphasizes two further arrivals: (1) a  $P$ - $P$  phase reflection ( $q = 4$ ) from the Moho at  $\sim 11$  s and (2) a weaker  $S$ - $P$  conversion ( $q = 5$ ) from the Moho at  $\sim 17$  s. These phases represent the dominant contributions to scattering; several other “kinematic analogues” involving interaction with the free surface may also be identified, but these represent effectively second-order contributions.

Figures 2c and 2d present the corresponding displacement components for a plane wave incident from the left. The amplitudes of converted phases ( $q = 2, 4, 5$ ) from the near-planar horizons are diminished with respect to Figures 2a and 2b because the specular angles are closer to  $0^\circ$  (and hence the conversion coefficients are closer to zero), while diffracted signals from the suture are more pronounced. A series of diffractions, all centered near  $\sim 150$  km in offset, are apparent: (1) a  $P$ - $P$  diffraction ( $q = 1$ ) with apex at  $\sim 0$  s (Figure 2d)); (2) two  $P$ - $S$  diffractions ( $q = 2$ ) with apices at  $\sim 5$  s and  $\sim 7$  s (Figure 2c)); (3) a  $P$ - $P$  diffraction ( $q = 3$ ) with apex at  $\sim 10$  s (Figure 2d)); and (4) a  $S$ - $P$  diffraction ( $q = 5$ ) with apex at  $\sim 16$  s (Figure 2d).

## 5. Migration/Inversion Method

Our intent in this section is to summarize several key results from paper 1 and to amend them slightly to forms appropriate for the in-plane geometry of the present problem. The most obvious simplification involves the restriction of all vector quantities (e.g., filtered, scattered displacement  $\mathbf{v}$ , incident slowness  $\mathbf{p}^0$ , scattered slowness  $\mathbf{p}^S$ ) to the  $x_1, x_3$  plane. Accordingly, equation (39) of paper 1 is rewritten as

$$g_r(\mathbf{x}) = \int dp_1^0 \int dx_1' \left| \frac{\partial(\psi, \theta)}{\partial(x_1', p_1^0)} \right| \sum_q W_r^q(x_1', p_1^0, \mathbf{x}) \frac{|\nabla T^q|^2}{|A^q|^2} \cdot \sum_n A_n^q(\mathbf{x}, \mathbf{x}') v_n^q(\mathbf{x}', p_1^0, t = T^q), \quad (1)$$

where  $W_r^q$  describes the radiation pattern for a particular scattering mode  $q$  and material perturbation  $r$ ,  $\nabla T^q$  is the spatial gradient of the total travel time function evaluated with respect to the scattering point  $\mathbf{x} = (x_1, x_3)$ , and  $|A^q|^2 = \sum_n A_n^q A_n^q$ , where  $A_n^q$  accounts for the predicted geometrical amplitude and polarity of the scattered mode  $q$ . Note that the integration over sources is now cast in terms of the Cartesian horizontal slowness  $p_1^0$  rather than its absolute value  $|\mathbf{p}_1^0| = \sqrt{(p_1^0)^2 + (p_2^0)^2}$  (compare paper 1). The Jacobian change of variables in (1) is altered by the loss of one degree of freedom in the data variables, and equation (B10) in paper 1 reduces to

$$\left| \frac{\partial(\psi, \theta)}{\partial(x_1', p_1^0)} \right| = \left| \frac{\cos\phi}{(J^S)^2} \frac{\alpha^0}{\sqrt{1 - (p_1^0)^2 (\alpha^0)^2}} \right|, \quad (2)$$

for a  $P$ - $S$  interaction, where  $\phi$  is the surface takeoff angle of the Green's function ray,  $\alpha^0$  is the  $P$  wave velocity of the 1-D reference medium, and  $J^S$  is the  $S$  wave geometrical spreading function between scatter point  $\mathbf{x} = (x_1, x_3)$  and receiver location  $\mathbf{x}' = (x_1', 0)$ . The Jacobian is modified from (2) when considering other scattering interactions by (1) a replacement of  $J^P$  for  $J^S$  for modes  $q = 1, 3, 5$  and (2) a substitution of the reference, shear velocity  $\beta^0$  for  $\alpha^0$  for modes  $q = 5, 6$ . With these modifications the material property perturbations at any particular scatter point,  $\Delta\mathbf{m}(x_1, x_3) = [\Delta\alpha/\alpha^0, \Delta\beta/\beta^0, \Delta\rho/\rho^0]$ , are retrieved through a trivial  $3 \times 3$  matrix inversion and multiplication as

$$\Delta\mathbf{m} = \mathbf{H}^{-1}\mathbf{g}, \quad (3)$$

where the three elements of  $\mathbf{g}$  are obtained from (1) and  $\mathbf{H}$ , following equation (41) of paper 1, is given by

$$H_{rs}(\mathbf{x}) = \int dp_1^0 \int d\theta \sum_q W_r^q(\theta, p_1^0, \mathbf{x}) W_s^q(\theta, p_1^0, \mathbf{x}). \quad (4)$$

where the dependence of  $W_r^q$  on  $\theta$ ,  $p_1^0$ , and  $\mathbf{x}$  is explicitly identified.

Equation (1) is akin to the diffraction stack of classical migration and defines the potential function  $g_r(\mathbf{x})$ , at any model point  $\mathbf{x}$ , as a weighted summation over all receivers and events of the data along predicted travel time curves for the particular mode interaction  $q$  as determined for the smoothly varying, 1-D reference medium. Computation of (1) and (4) is performed individually for all model points. Examples of travel time curves for the different scattering modes are superposed on Figures 2a–2d for a model point  $\mathbf{x} = (240 \text{ km}, 40 \text{ km})$  at Moho depth. The scattered wave travel times  $T^q$ , normalized with respect to the direct  $P$  arrival, are easily calculated for a 1-D reference model. For a direct  $P$ - $S$  conversion ( $q = 2$ ) we have

$$T^{(2)}(\mathbf{x}, x_1', p_1^0) = \int_0^{x_3} \frac{dy_3}{\beta(y_3) \sqrt{1 - \beta^2(y_3) (p_1^S)^2}} - p_1^0 (x_1' - x_1) - \int_0^{x_3} \frac{dy_3}{\alpha(y_3) \sqrt{1 - \alpha^2(y_3) (p_1^0)^2}}, \quad (5)$$

where  $p_1^S$  is the horizontal slowness of the ray traveling between scatter point  $\mathbf{x} = (x_1, x_3)$  and receiver  $\mathbf{x}' = (x_1', 0)$ . For a direct  $P$ - $P$  interaction ( $q = 1$ ),  $p_1^P$  (horizontal slowness of the scattered  $P$  wave) and  $\alpha^0$  are substituted for  $p_1^S$  and  $\beta^0$ , respectively.

When calculating the expected arrival times for backscattered waves, we must account for the extra time incurred by a wave traveling to surface and returning to the scatterer point and for the possibility of  $P$ - $S$  conversion at the free surface. Thus the expected travel time for, e.g., a backscattered  $P$ - $P$  ( $q = 3$ ) interaction, is

$$T^{(3)}(\mathbf{x}, x_1', p_1^0) = \int_0^{x_3} \frac{dy_3}{\alpha(y_3) \sqrt{1 - \alpha^2(y_3) (p_1^P)^2}} - p_1^0 (x_1' - x_1) + \int_0^{x_3} \frac{dy_3}{\alpha(y_3) \sqrt{1 - \alpha^2(y_3) (p_1^0)^2}}. \quad (6)$$

Travel times for other phases are calculated after slight modification: (1)  $P$ - $S$  scattering ( $q = 4$ ) requires substitutions of  $p_1^S$  and  $\beta$  for  $p_1^P$  and  $\alpha$  in the first term; (2) for  $S$ - $P$  scattering ( $q = 5$ ),  $\alpha^0$  is replaced by  $\beta^0$  in the third term; and (3)  $S$ - $S$  scattering ( $q = 6$ ) requires all three of the substitutions in points 1 and 2.

Two further points are worth noting. First, the travel times of scattered modes which share similar polarizations at the receiver differ only by static time shifts for the 1-D reference model. Second, asymmetries about the scatter point exist in the travel time move out with distance which result from the  $p_1^0$  dependence in (5) and (6) as manifest by skew in the hyperbolae in Figures 2a–2d. In particular, we note that the expected travel time move out for, e.g., a forward scattered  $P$ - $S$  interaction in a 1-D medium, is

$$\frac{\partial T^{(2)}}{\partial x_1'}(\mathbf{x}, x_1', p_1^0) = -p_1^0 + \frac{\partial p_1^S}{\partial x_1'} \int_0^{x_3} dy_3 \frac{\beta^0(y_3) p_1^S}{[1 - [\beta^0(y_3)]^2 (p_1^S)^2]^{\frac{3}{2}}}. \quad (7)$$

## 6. Numerical Simulations

The inversion methodology described in section 5 is now applied to the synthetic data sets in a series of investigations to assess its potential and limitations. We begin with an exami-

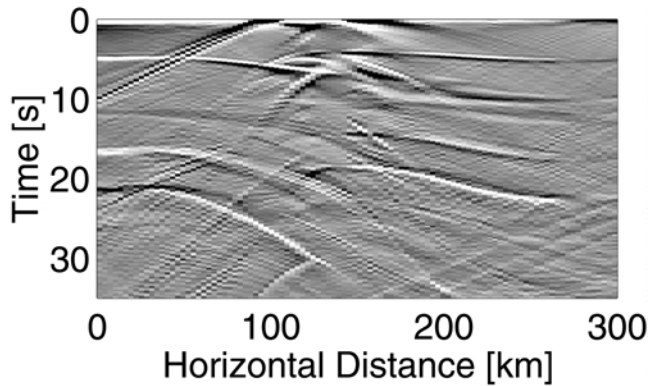


**Figure 3.** Receiver function image constructed through simultaneous, least squares deconvolution of individual  $S$  wave traces by corresponding  $P$  wave traces for all six suites of seismograms.

nation of the imaging potential of forward scattered modes from single events. Subsequently, all forward scattered  $P$ - $S$  responses are combined in a single inversion to gage the improvements resulting from enhanced source coverage. The remaining modes are then investigated to compare differences in resolution between forward scattered and backscattered interactions. Following this, a majority of scattering interactions from all events are combined to further improve the reconstruction of subsurface discontinuous structure. The section concludes with an analysis of the degradation accruing from the introduction of noise and reduced station sampling.

In the examples that follow, our choice of 1-D reference model consists of a 40-km-thick crust overlying an upper mantle half-space. Velocities and densities of these two reference materials are identical to the crustal and mantle properties specified in the first two rows of Table 1. In addition, we invert only for  $\Delta\alpha/\alpha^0$  and  $\Delta\beta/\beta^0$ , the two most linearly independent parameters in the case of forward scattering [e.g., *Bostock and Rondenay, 1999*], since the third parameter (i.e.,  $\Delta\rho/\rho^0$ ) remains effectively indeterminate for surface receiver arrays. In situations where backscattering is represented, we recognize that this is not the best choice of parameter combination [see, e.g., *Forgues and Lambaré, 1997*]. However, *Forgues and Lambaré [1997]* demonstrate that any choice of parameterization may be simply recovered through matrix multiplications after inversion. Thus, for simplicity, all inversion results are presented in terms of the physically meaningful, though not always optimal, velocity perturbations.

Before we proceed to detail individual simulations, it is desirable to present a basis for comparison between our inversion methodology and conventional teleseismic processing. A receiver function image [e.g., *Langston, 1979*] constructed via simultaneous, least squares deconvolution [e.g., *Gurrola et al., 1995*] of individual  $S$  wave traces by corresponding  $P$  wave traces (as determined in step 1 of the preprocessing sequence) from all six events is shown in Figure 3. Well-defined  $P$ -to- $S$  conversions from the Moho and subducted crust are apparent to the left and right of the suture. However, traces to the left side of the section and near the suture at offsets of  $\sim 120$  km are corrupted by strong forward scattered  $P$ - $P$  and  $P$ - $S$  diffraction energy (see data sections in Figure 2). Free-surface multiples corresponding to interactions  $q = 3,4,6$  are evident at times later than 10 s and may be potentially misinterpreted as deeper structure. We expect that a formal, multiple-mode inversion will significantly reduce these contaminating artifacts and allow for an improved imaging of more complex structure.

### 6.1. Simulation 1: Single-Event Inversion of Forward Scattering Modes

To examine the bias resulting from source direction, forward scattering modes  $q = 1, 2$  are inverted separately for two events with positive ( $p_1^0 = 0.07$  s km $^{-1}$ ) and negative ( $p_1^0 = -0.07$  s km $^{-1}$ ) horizontal slowness (Figures 4 and 5, respectively). Because of the limited sampling afforded by a single event we will restrict recovery to a single material parameter for both modes using the Jacobian,  $|\partial\psi/\partial x_1^0|$ , in (B11) of paper 1. In particular, we consider the perturbations  $\Delta\alpha/\alpha^0$  for  $q = 1$  and  $\Delta\beta/\beta^0$  for  $q = 2$  as optimal choices for forward scattering. The  $P$  velocity perturbations reconstructed from the forward scattered  $P$ - $P$  ( $q = 1$ ) interaction are presented in Figure 4a. Vertical streaking about the suture zone with the correct general polarity is observed though little focusing of energy is achieved.  $S$  velocity perturbations recovered by the direct  $P$ - $S$  ( $q = 2$ ) interaction (Figure 4b) afford a much better delineation of the normal-relict crustal boundary. Note that apart from this boundary, little of the remaining, more planar components of structure is reconstructed.

Figures 5a and 5b present the same parameter and mode interaction combinations as Figures 4a and 4b but for an incident wave with slowness  $-0.07$  s km $^{-1}$ . Figure 5a shows increased streaking about the suture zone, relative to Figure 4a, and a correlation with actual structure that is poorer still. Unlike Figure 4b, the  $S$  velocity image in Figure 5b reconstructs the relict crust-mantle boundaries (though displaced upward from their true locations) but identifies little contrast with adjacent normal crust. The Moho is now more prominent, though its location is slightly displaced from the known lithospheric model. The mislocation of structure is related to the inadequacy of the 1-D reference velocity model in correctly predicting the travel times of scattered phases. Where Moho depths are  $<40$  km, there is a corresponding “pull up” of underlying structure, while the converse is true in areas where the Moho exceeds 40 km depth.

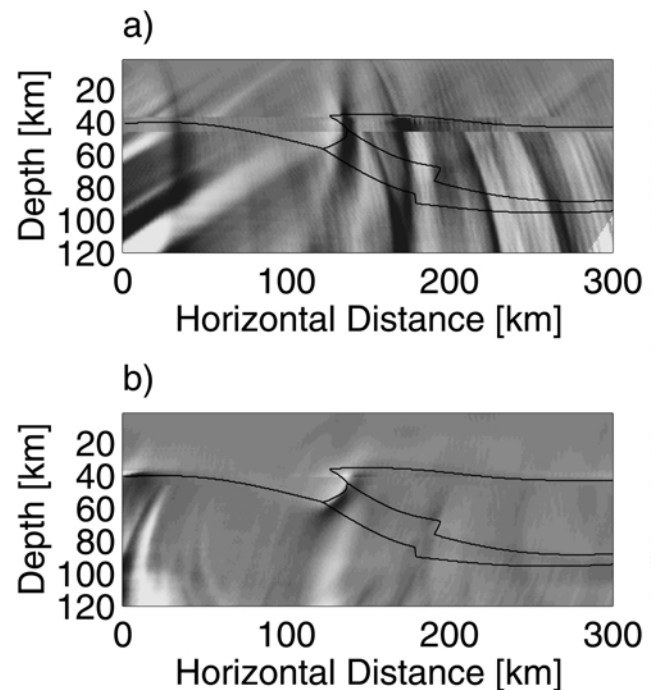


**Figure 4.** Reconstructed velocity perturbations from inversion of forward scattered modes for a left-incident plane wave field ( $p_1^0 = 0.07$  s km $^{-1}$ ). (a)  $\Delta\alpha/\alpha^0$  from  $q = 1$ ; and (b)  $\Delta\beta/\beta^0$  from  $q = 2$ .

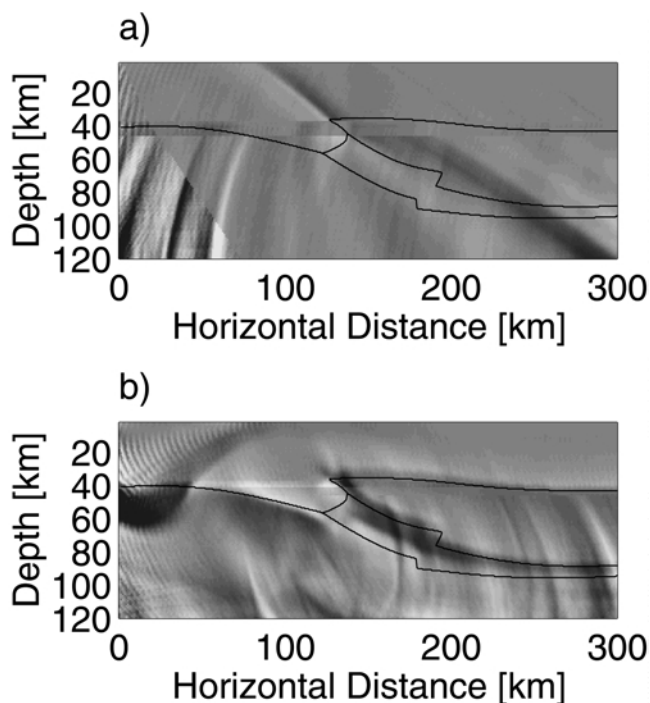


**Figure 5.** Reconstructed velocity perturbations from inversion of forward scattered modes for a right-incident plane wave field ( $p_1^0 = -0.07 \text{ s km}^{-1}$ ). (a)  $\Delta\alpha/\alpha$  from  $q = 1$ ; and (b)  $\Delta\beta/\beta^0$  from  $q = 2$ .

The present simulation serves to illustrate several of the shortcomings inherent in single-mode inversions in general and forward scattering inversions in particular. Of specific note is the poor recovery of structure in the forward scattered  $P$ - $P$  images (Figures 4a and 5a). The origin of this lack of sensitivity can be traced to the factor  $|\nabla T^q|^2$  that appears in (1) and weights the diffraction stack according to the sensitivity of total travel time to scatterer location. For  $q = 1$  in the strictly forward scattering direction ( $\theta = 180^\circ$ ) the sensitivity is zero, as discussed extensively by *Marquering et al.* [1999], and remains relatively small for a range of angles about the forward direction. A consequence of this behavior is that considerable trade-off exists between the lateral extent of the scattering body and its depth in near-forward directions. This effect is manifest in the diffuse appearance of reconstructed anomalies in Figures 4a and 5a.

A second issue worth noting is the contrasting recovery of structure for events with differing horizontal slowness. In general, the successful reconstruction of a material property perturbation is dependent upon the strength of the associated scattered response. In the case of extended, quasi-planar discontinuities separating gently varying media this scattered response will be most pronounced in directions corresponding to the specular angle of interaction. For  $P$ -to- $S$  conversions ( $q = 2$ ), however, we must also consider the effect of conversion coefficients which tend to zero as the specular angle approaches  $0^\circ$  (i.e., normal incidence). In this case, the incident wave field has little sensitivity to structure since no  $P$ - $S$  scattering results. Consequently, the structure can be regarded as falling within the null-space of the problem and will not be recovered within the inversion.

These effects are well illustrated in Figures 4b and 5b. In the case of left incidence (Figures 2c and 2d),  $P$ - $S$  ( $q = 2$ ) scattering from the subhorizontal boundaries is weak since the incoming wave field is incident at near-normal angles. The sole exception is the short boundary segment between normal and relict crust which is sufficiently limited and oblique to generate strong diffractions.

Consequently, only the latter feature is well resolved in Figure 4b. In contrast, illumination of the lithospheric section by a plane wave from the right (Figures 2a and 2b) produces stronger  $P$ - $S$  conversions from the near-planar structures as they are oriented at more oblique angles to the incident wave. Accordingly, Figure 5b documents an improved reconstruction of the Moho and the lateral extent of subducted relict crust.

## 6.2. Simulation 2: Multiple Event Inversion of Forward Scattering Modes

We now investigate the effect of simultaneous inversion of multiple events on the reconstruction of material properties. In this simulation and those that follow, we employ the Jacobian change of variables in (2) as a range of incident slowness  $p_1^0$  is now sampled. The reconstructed  $P$  and  $S$  velocity images from the inversion of all six forward scattered  $P$ - $P$  and  $P$ - $S$  interactions are presented in Figures 6a and 6b, respectively. As might be expected, the image in Figure 6b combines the structural features imaged separately in Figures 4b and 5b. In particular, all of the boundaries which define the suture are now well resolved. Perturbations across the Moho, in particular, are retrieved at laterally coherent levels along the entire breadth of the array. However, in a comparison with the known model structure we note that the amplitude of the reconstructed Moho discontinuity is underestimated relative to the short-wavelength suture. This is due, in part, to incomplete coverage in angular coverage in  $\nabla T^q$ , as we shall discuss further in section 6.3. It is also worth noting that some contamination from scattered  $P$ - $P$  ( $q = 1$ ) enters the image at shallow crustal levels.

Figure 6a documents little improvement over Figures 4a and 5a in the recovery of discontinuous structure. In contrast to Figure 6b, recovered perturbation magnitudes are  $<50\%$  of the known jumps in material properties and show poor correlation with the true structure. This result is thought to be due to a combination of relative insensitivity of the forward scattered  $P$ - $P$  mode to structural location and a distortion of the actual scattered  $P$  wave field

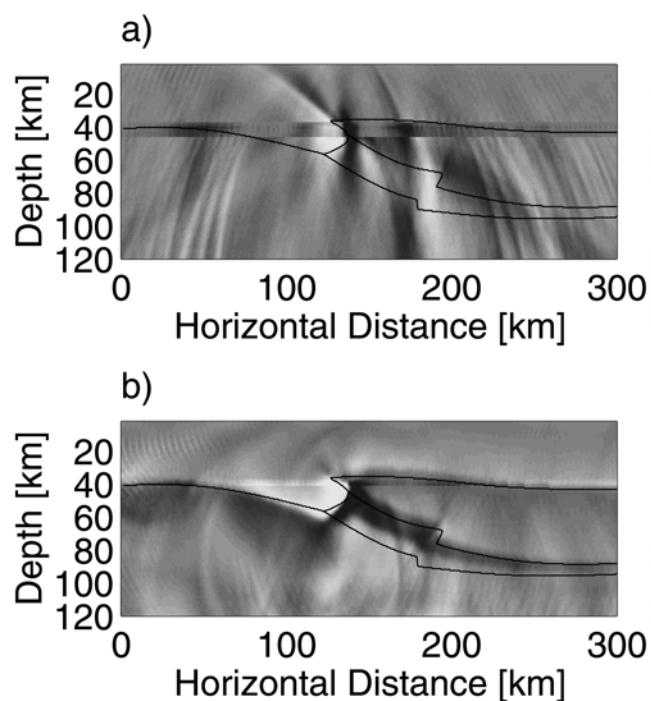


**Figure 6.** Reconstructed velocity perturbations from inversion of forward scattered modes of all six incident plane wave fields. (a)  $\Delta\alpha/\alpha^0$  from  $q = 1$ ; and (b)  $\Delta\beta/\beta^0$  from  $q = 2$ .

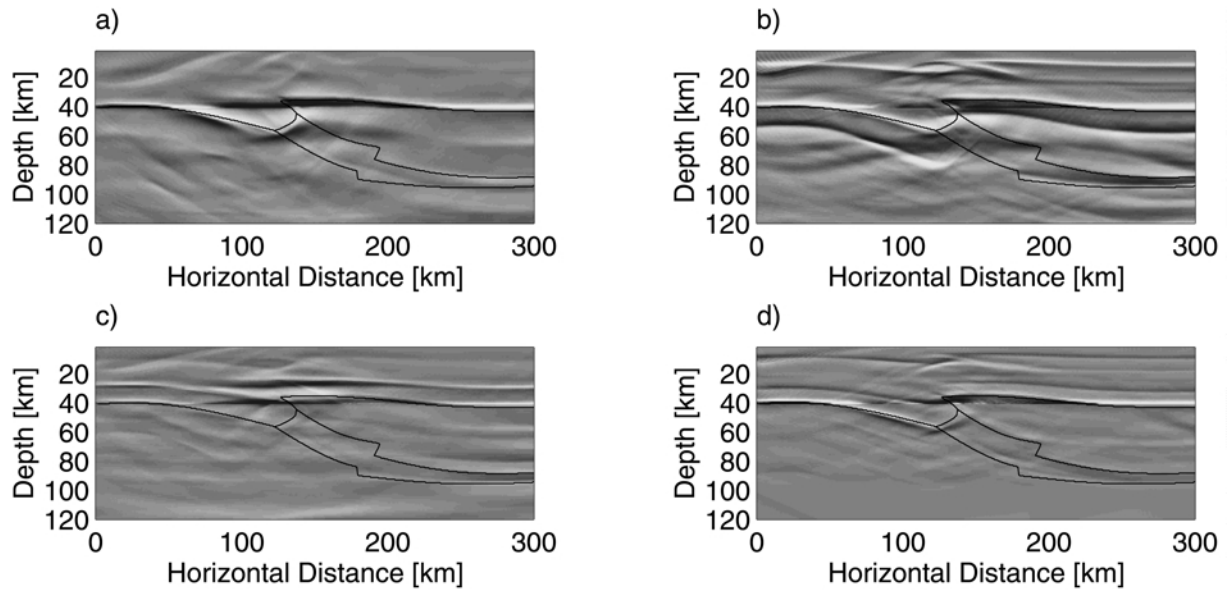


**Figure 7.** Reconstructed velocity perturbations from inversion of individual backscattered modes for all six incident plane wavefields. (a)  $\Delta\alpha/\alpha^0$  from  $q = 3$ ; (b)  $\Delta\beta/\beta^0$  from  $q = 4$ ; (c)  $\Delta\beta/\beta^0$  from  $q = 5$ ; and (d)  $\Delta\beta/\beta^0$  from  $q = 6$ .

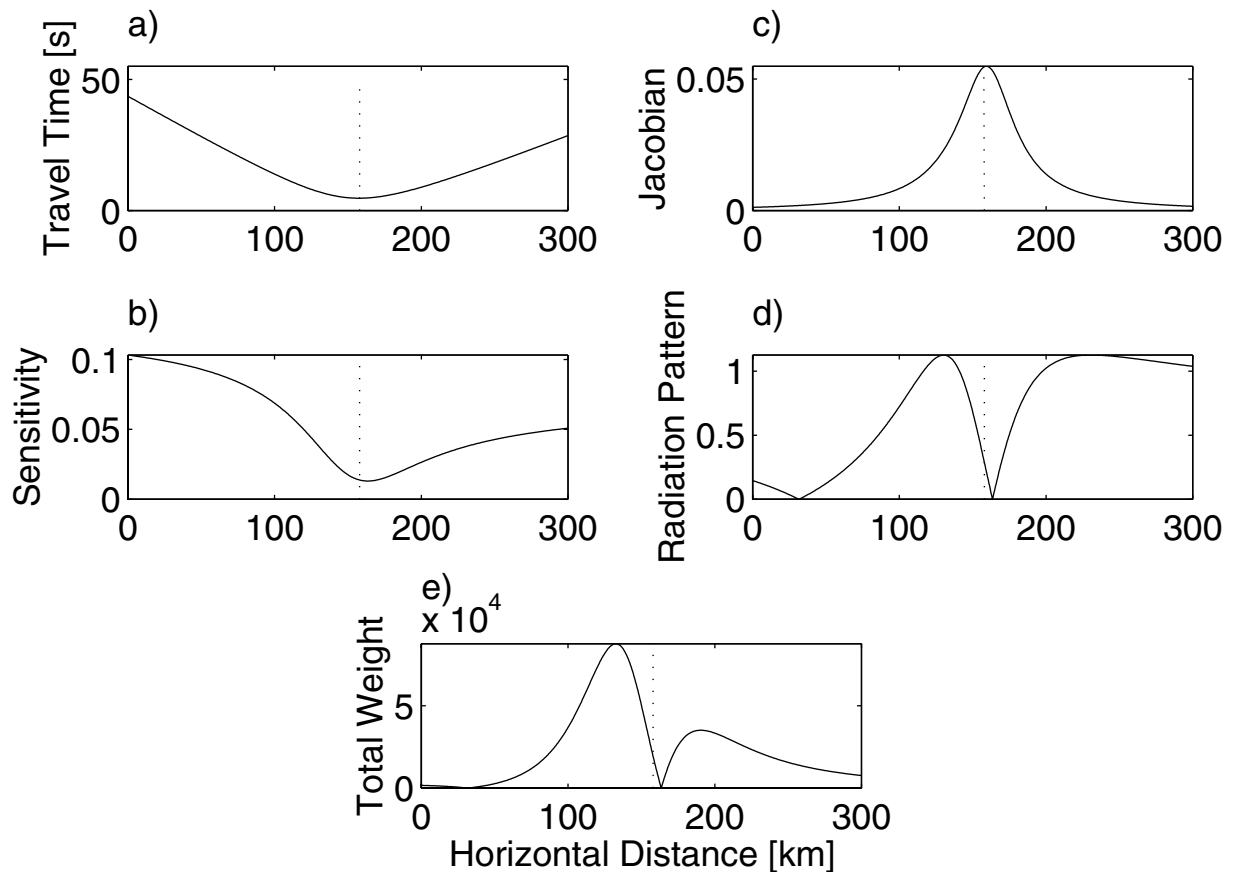


**Figure 8.** Diffraction stack weights for forward scattered  $P$ - $S$  interaction ( $q = 2$ ). (a) Total travel time  $T^{(2)}$ ; (b) travel time sensitivity  $|\nabla T^{(2)}|^2$ ; (c) Jacobian of the transformation of variables  $|\partial\psi/\partial x'_1|$ ; (d) radiation pattern  $W_2^2$ ; and (e) product of Figures 8b, 8c, and 8d.

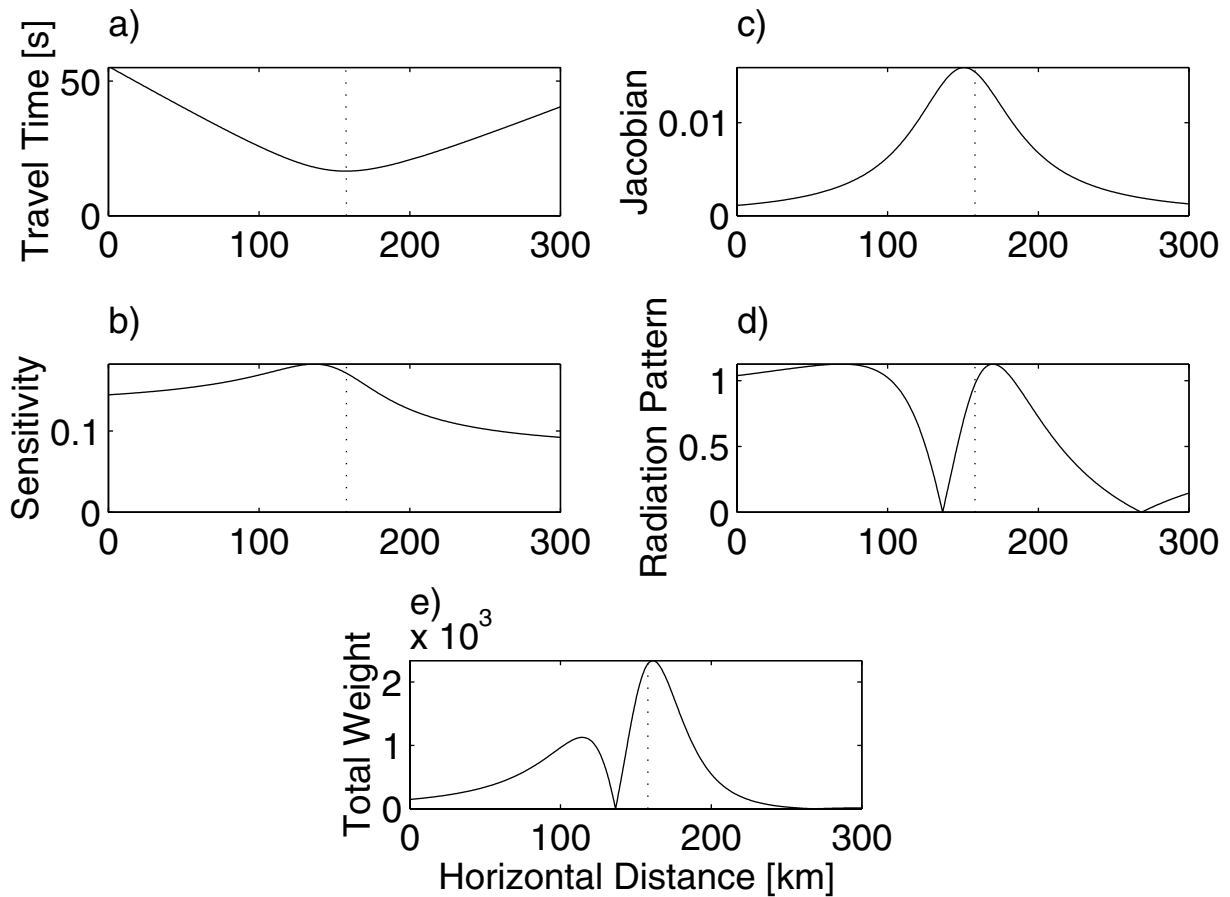


**Figure 9.** Diffraction stack weights for backscattered  $P$ - $S$  interaction ( $q = 4$ ). (a) Total travel time  $T^{(4)}$ ; (b) travel time sensitivity  $|\nabla T^{(4)}|^2$ ; (c) Jacobian of the transformation of variables  $|\partial\psi/\partial x'_1|$ ; (d) radiation pattern  $W_2^4$ ; and (e) product of Figures 9b, 9c, and 9d.

incurred during preprocessing. Accordingly, we will refrain from using this mode in further inversions.

### 6.3. Simulation 3: Multiple-Event, Backscattered Mode Inversion

In this section, we apply the inversion procedure to backscattered modes  $q = 3, 4, 5, 6$  (Figures 7a–7d) from all six incident wave fields. Figure 7a presents the reconstructed  $P$  velocity perturbations for the  $P$ - $P$  ( $q = 3$ ) reflection. In this image the Moho and normal-relict crustal boundary are accurately delineated with locations that correspond well with the actual model. In particular, the localization and placement of these discontinuities are enhanced relative to those of the forward scattering inversions. This improvement is directly attributable to the increased sensitivity of backscattered travel time variations to scatterer location as represented by  $|\nabla T^q|^2$  in (1) and discussed in paper 1. Figure 7b presents the  $S$  velocity perturbations recovered from the  $P$ - $S$  ( $q = 4$ ) reflection. The Moho is once more well defined and is less smeared near the suture zone than in Figure 7a. The two discontinuous interfaces of the relict crust are also apparent and indicate the presence of a high-velocity anomaly. Later arriving energy from the  $S$ - $S$  ( $q = 6$ ) reflection contaminates the image at depths of  $\sim 60$  km.  $S$  velocity perturbations retrieved from the  $S$ - $P$  ( $q = 5$ ) reflection are shown in Figure 7c. The strongest anomaly is located at mid-lower crustal depths and indicates that the image is strongly contaminated by the earlier and stronger  $P$ - $P$  ( $q = 3$ ) reflections.  $S$  velocity

perturbations retrieved by the  $S$ - $S$  ( $q = 6$ ) interaction (Figure 7d) document a good recovery of the Moho and suture. Earlier  $P$ - $S$  energy is erroneously mapped to depths near  $\sim 30$  km. We remark that, in general, backscattered modes are observed to effectively resolve laterally discontinuous structure at levels commensurate with the true velocity model but that artifacts caused by the misidentification of other phases are more prevalent than in Figure 6.

An assumption inherent in the methodology is that individual scattering modes have been isolated prior to data input. In practice, this assumption can only be realized insofar as scattering modes ending as  $P$  or  $S$  waves can be separated on the basis of approximately orthogonal polarizations. Therefore an obvious complication is the degree to which single-mode reconstructions are contaminated by energy from other scattering interactions of similar wave type. For example, over the range of horizontal slowness utilized in these investigations, the free-surface-corrected amplitudes of  $S$ - $S$  reflections from the Moho are only slightly larger ( $\sim 30\%$ ) than those for  $P$ - $S$  reflections. Since these phases possess similar amplitudes, both yield accurate estimates of the jumps in material properties across the Moho. However, each phase also contributes to phantom structure in the other image. This situation also exists for  $P$  waves, though, in this case the amplitudes of  $P$ - $P$  reflections outweigh those of  $S$ - $P$  by a factor of  $\sim 4$ . As a result, the backscattered  $S$ - $P$  interaction is far less effective in the imaging process. As we show in section 6.4, the problem of mode inseparability is partially offset through simultaneous inversion of all modes; however, it is important for confident

interpretation that individual mode inversions are examined at this stage for features common to all images.

Although the appearance of forward scattered and backscattered phases on seismograms (e.g.,  $P$ - $S$  interactions  $q = 2, 4$  in Figure 2) is quite similar (aside from the static time shifts), they produce rather different images. In particular, we note that the jump across the Moho in the forward scattering reconstruction is rather more diffuse and downweighted relative to shorter-wavelength structure than for backscattered modes. An understanding of this behavior requires that we examine the contributions from different factors ( $W_r^q(\theta)$ ,  $|\nabla T^q|^2$ ,  $|\partial\psi/\partial x'_1|$ ) that weight the diffraction stack. These quantities and their product are presented in Figures 8 and 9 for modes  $q = 2, 4$ , respectively. The depth of the scatterer point under consideration is 40 km, and the slowness of the incident wave is  $0.05 \text{ s km}^{-1}$ . For reference, the location of the travel time minimum is shown in Figures 8 and 9 as a dotted line.

Figures 8b and 8d show the travel time sensitivity  $|\nabla T^{(2)}|^2$  and radiation pattern  $W_2^2(\theta)$  factors. Both factors contribute to significant downweighting near the travel time apex, whereas the Jacobian of the transformation of variables,  $|\partial\psi/\partial x'_1|$  (Figure 8c), is sharply peaked and maximally weights the diffraction stack close to the minimum travel time. The cumulative product that represents the total weight along the diffraction stack is bimodal with the travel time apex falling away from the global minimum such that at the apex the diffraction stack receives only  $\sim 25\%$  of the maximum weight. In the case of  $P$ - $S$  backscattering ( $q = 4$ ) (Figure 9), travel time sensitivity and radiation pattern are more favorably positioned in Figure 9b and 9d such that the maximum of the total weighting function is closer to the apex of  $T^{(4)}$ . The Jacobian (Figure 9c) is slightly broadened relative to that in Figure 8c. Consequently, the cumulative weighting function (Figure 9e) is again bimodal, but the  $T^{(4)}$  apex is now positioned close to the location of maximum weight.

While these weights are appropriate and effective for single, point scatterers, they have a rather different efficiency for quasi-planar structures. Since the diffraction hyperbolae are tangent to the travel time loci for planar discontinuities at the hyperbola apex, reconstruction using forward scattered energy extracts a lower proportion of signal from the true arrival. It is therefore more prone to contamination from noise and may be more susceptible to incomplete angular coverage (i.e.,  $\psi$ ) in  $\nabla T^q$ .

#### 6.4. Simulation 4: Multiple-Mode, Multiple-Event Inversion

In this simulation the improvements in model reconstruction incurred through simultaneous inversion of both forward scattered and backscattered modes ( $q = 2, 3, 4, 6$ ) are examined. As mentioned above, the inability to fully separate individual scattering modes results in images that suffer from cross-mode contamination (compare simulation 3). Therefore it is justified to weight individual mode contributions in the simultaneous inversion on some a priori basis which accounts for this contamination. In particular, relative signal amplitudes as governed by free-surface reflection coefficients and the anticipated response of underlying heterogeneity must be considered. In the present simulation these factors have been considered in a somewhat subjective fashion and have been chosen so as (1) to downweight the  $P$ - $S$  ( $q = 4$ ) interaction by 30% to bring the contaminating  $S$ - $S$  ( $q = 6$ ) interaction structure to approximately comparable levels with the  $P$ - $S$  ( $q = 4$ ) phantom structure observed in the  $S$ - $S$  ( $q = 6$ ) interaction image and (2) to upweight the forward scattered  $P$ - $S$  ( $q = 2$ ) interaction by a factor of 6 to allow for a more balanced representation of forward scattering in the simultaneous inversion results.

Figures 10a and 10b present the reconstructed  $P$  and  $S$  velocity perturbations from the inversion of the four individually weighted modes, respectively. In both Figures 10a and 10b the Moho and the relict crust are well delineated in reference to

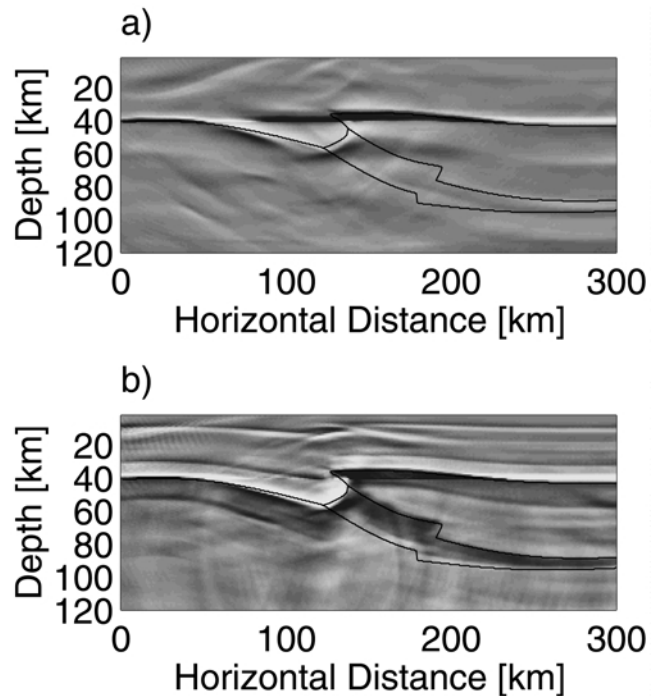


**Figure 10.** Reconstructed velocity perturbations from simultaneous inversion of individually weighted modes from all six events. (a)  $\Delta\alpha/\alpha^0$ ; and (b)  $\Delta\beta/\beta^0$ .

model structure. In accordance with the true velocity model (see Table 1) the  $S$  velocity image identifies the relict crust as a relatively larger perturbation than its  $P$  velocity counterpart. Furthermore, in contrast with the images recovered from individual backscattered waves (i.e., simulation 3), the resulting  $S$  velocity perturbation image is now less contaminated by phantom structure leaving the suture zone more clearly evident. In general, the simultaneous inversion of individually weighted scattering interactions realizes a well-constrained, improved reconstruction of the model.

#### 6.5. Simulation 5: Random Noise and Spatial Aliasing Issues

Simulations 1–4 have employed noise-free data sets to investigate the inversion/migration methodology developed in paper 1. The ability of the approach to perform in a situation where data quality and recording geometry are more representative of typical field simulations is now examined. The idealized suture model has been altered to include a surface layer of 6-km average thickness (Figure 11a). The layer is characterized by  $P$  and  $S$  velocities and density of  $5.2 \text{ km s}^{-1}$ ,  $2.8 \text{ km s}^{-1}$ , and  $2.5 \text{ g cm}^{-3}$ , respectively, and exhibits undulations of maximum amplitude of 1.2 km which give rise to near-surface body wave and surface wave scattering (see Figures 11b and 11c). In addition, a random selection of 60 stations has been taken from the previous 120 stations, resulting in receiver spacing between 3 and 15 km, and data sections have been contaminated with Gaussian noise of zero mean and a standard deviation equivalent to 5% of the amplitude of the incident wave. Given the frequency content of the incident wave field, it is expected that the resulting images will suffer to some degree from the effects of spatial aliasing.

Figures 11d and 11e present the  $P$  and  $S$  velocity images using the same weighted mode contribution and event selection as in simulation 4. In both images the Moho and normal-relict crustal discontinuities remain well delineated. The  $S$  velocity image also accurately retrieves the remaining discontinuities of the suture zone. Scattering from the near-surface layer has introduced to the images an additional source of noise that

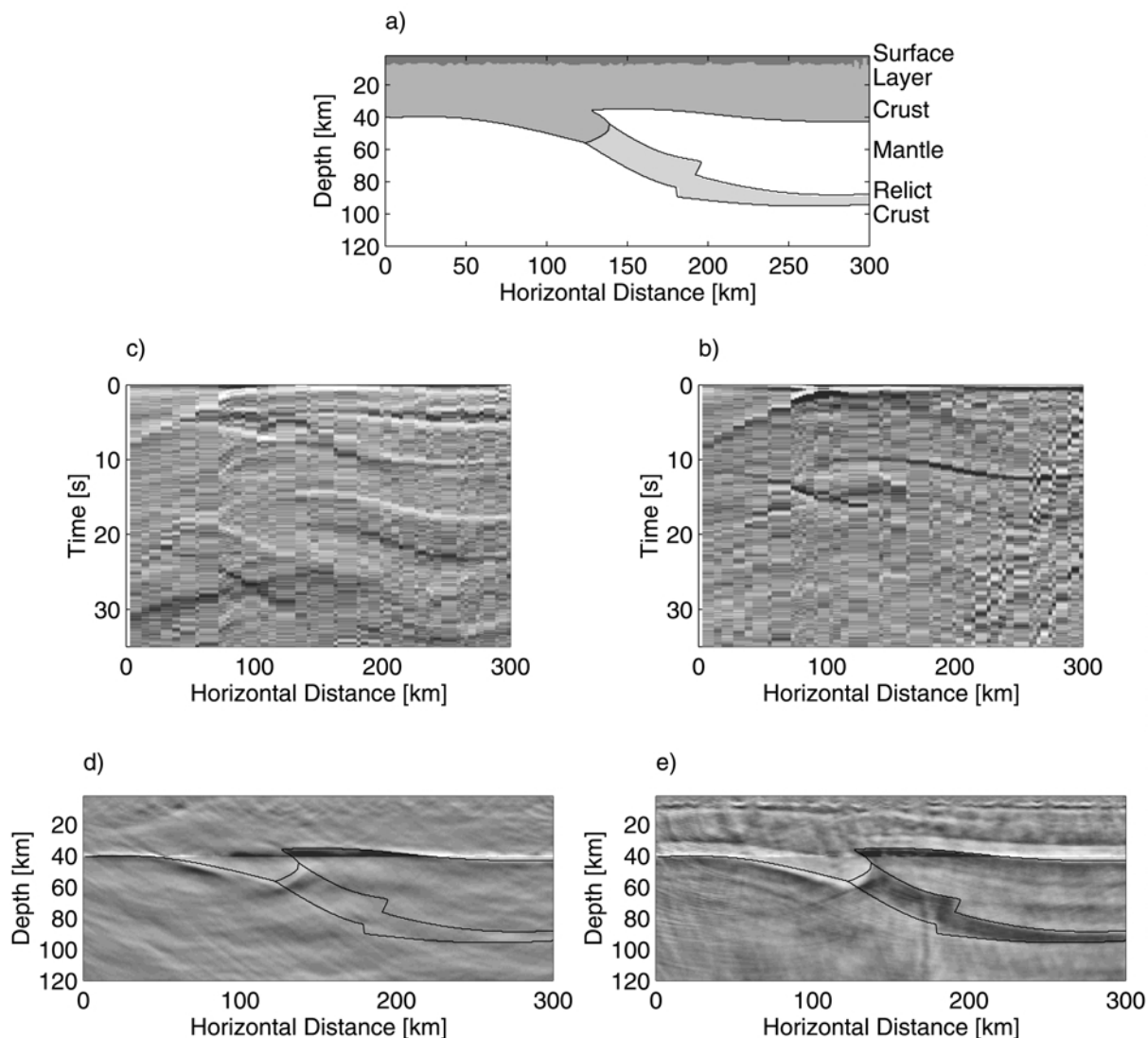


**Figure 11.** Reconstructed velocity perturbations from simultaneous inversion of individually weighted modes from all events including correlated and additive noise and reduced irregular station spacing. (a) Revised model including laterally varying, near-surface layer; (b)  $\Delta u_1$ , and (c)  $\Delta u_3$  components for an incident plane wave with horizontal slowness  $p_1^0 = -0.07 \text{ s km}^{-1}$ , (d)  $\Delta\alpha/\alpha^0$ , and (e)  $\Delta\beta/\beta^0$ .

has been mapped back to the near surface. Additive white noise has had a relatively minor effect on the reconstruction since it is largely cancelled through the integration in (1). Figures 11d and 11e do suffer from spatial aliasing manifest through high wave number “speckle” which is, however, most prominent at shallow levels and diminishes with depth so as not to pose significant impediment in the reconstruction of lower crustal and mantle structures.

## 7. Concluding Remarks

In this paper, we have presented results from a number of synthetic simulations that test the inversion/migration methodology developed in paper 1. We have exploited the flexibility of the method to investigate the roles that different scattering mode and event combinations play in the recovery of structure corresponding to an idealized lithospheric suture. In particular, we have demonstrated (1) the contrasting and somewhat complementary sensitivity of forward scattered and backscattered modes

to structure, (2) the reduction in problem null-space that accompanies increased source coverage, (3) improvements in structural recovery incurred through simultaneous treatment of different scattering modes, and (4) the robustness of the approach in the presence of typical signal-to-noise levels and irregular station geometry. In the final paper of the series (paper 3) we investigate the application of the method to field data recorded over the Cascadia subduction zone.

**Acknowledgments.** We gratefully acknowledge the constructive criticisms of referees Guust Nolet and Gary Pavlis and Associate Editor Justin Revenaugh. This research was supported by NSERC (Natural Sciences and Engineering Research Council of Canada) research grant OGP0138004.

## References

Beylkin, G., and R. Burridge, Linearized inverse scattering problem by inversion of a causal generalized Radon transform, *Wave Motion*, 12, 15–52, 1990.

- Bostock, M. G., Mantle stratigraphy and evolution of the Slave province, *Geophys. J. Int.*, *134*, 21,183–21,200, 1998.
- Bostock, M. G., and S. Rondenay, Migration of scattered teleseismic body waves, *Geophys. J. Int.*, *137*, 732–746, 1999.
- Bostock, M. G., S. Rondenay, and J. Shragge, Multiparameter two-dimensional inversion of scattered teleseismic body waves, 1, Theory of oblique incidence, *J. Geophys. Res.*, this issue.
- Cook, F. A., A. J. van der Velden, K. W. Hall, and B. J. Roberts, Tectonic delamination and subcrustal imbrication of the Precambrian lithosphere in northwestern Canada mapped by LITHOPROBE, *Geology*, *26*, 839–842, 1998.
- Forgues, E., and G. Lambaré, Parameterization study for acoustic and elastic ray + Born inversion, *J. Seismic Explor.*, *6*, 253–277, 1997.
- Gurrola, H., G. E. Baker, and J. B. Minster, Simultaneous time-domain deconvolution with application to the computation of receiver functions, *Geophys. J. Int.*, *120*, 537–543, 1995.
- Kennett, B. L. N., The removal of free surface interactions from three-component seismograms, *Geophys. J. Int.*, *104*, 153–163, 1991.
- Kosloff, D., D. Kessler, A. Q. Filho, E. Tessmer, A. Gehlle, and R. Strahilevits, Solutions of the equations of dynamic elasticity by a Chebyshev spectral method, *Geophysics*, *55*, 734–748, 1990.
- Langston, C. A., Structure under Mount Rainier, Washington, inferred from teleseismic body waves, *J. Geophys. Res.*, *84*, 4749–4762, 1979.
- Marquering, H., F. A. Dahlen, and G. Nolet, Three-dimensional sensitivity kernels for finite-frequency traveltimes: The banana-doughnut paradox, *Geophys. J. Int.*, *137*, 805–815, 1999.
- Revenaugh, J., A scattered-wave image of subduction beneath the transverse ranges, *Science*, *268*, 1888–1892, 1995.
- Rondenay, S., M. G. Bostock, and J. Shragge, Multiparameter two-dimensional inversion of scattered teleseismic body waves, 3, Application to CASC93, *J. Geophys. Res.*, this issue.
- Ryberg, T., and M. Weber, Receiver function arrays: a reflection seismic approach, *Geophys. J. Int.*, *141*, 1–11, 2000.
- VanDecar, J. C., Upper-mantle structure of the Cascadia subduction zone from non-linear teleseismic travel-time inversion, Ph.D. thesis, 165 pp., Univ. of Wash., Seattle, June 1991.
- VanDecar, J. C., and R. S. Crosson, Determination of teleseismic relative phase arrival times using multi-channel cross correlation and least squares, *Bull. Seismol. Soc. Am.*, *80*, 150–169, 1990.

---

M. G. Bostock, Department of Earth and Ocean Sciences, University of British Columbia, 129-2219 Main Hall, Vancouver, British Columbia, Canada B6T 1Z4. (bostock@geop.ubc.ca)

S. Rondenay, Department of Geological Sciences, Brown University, Dept. Box 1846, Providence, RI 02912, USA. (rondenay@emma.geo.brown.edu)

J. Shragge, Hager GeoScience Inc., 596 Main Street, Woburn, MA 01801, USA.

(Received July 19, 2000; revised March 14, 2001; accepted June 9, 2001.)